MIT Open Access Articles

Investigation of the role of Ti oxide layer in the size-dependent superelasticity of NiTi pillars: Modeling and simulation

Citation: Qiao, Lei and Radovitzky, Raul. "Investigation of the Role of Ti Oxide Layer in the Size-Dependent Superelasticity of NiTi Pillars: Modeling and Simulation." Acta Materialia 61, no. 16 (September 2013): 6213–6221. © 2013 Acta Materialia Inc

As Published: http://dx.doi.org/10.1016/j.actamat.2013.07.004

Publisher: Elsevier

Persistent URL: http://hdl.handle.net/1721.1/108120

Version: Author's final manuscript: final author's manuscript post peer review, without publisher's formatting or copy editing

Massachusetts Institute of Technology

Investigation of the role of Ti oxide layer in the size-dependent superelasticity of NiTi pillars: modeling and simulation

Lei Qiao, Raul Radovitzky*

Department of Aeronautics and Astronautics, Massachusetts Institute of Technology, 77 Massachusetts Avenue, Cambridge, MA 02139, USA

Abstract

Recent compression tests of NiTi pillars of a wide range of diameters have shown significant size dependency in the strain recovered upon unloading. In this paper, we propose a numerical model supporting the previously proposed explanation that the external Ti oxide layer may be responsible for the loss of superelasticity in the small pillars. The shape memory alloy at the center of the pillar is described using a nonlocal superelastic model, whereas the Ti oxide layer is modeled as elastoplastic. Voigt-average analysis and finite element calculations of the tests are compared to experiments for the range of pillar sizes considered in the experiments. The simulation results also suggest a size-dependent strain hardening due to the constraint on the phase transformation effected by the confining Ti oxide layer.

Keywords: Shape memory alloys; Martensitic phase transformation; Size effects

*Corresponding author
  Email address: `rapa@mit.edu` (Raul Radovitzky)

1. Introduction

The unique feature of shape recovery upon thermomechanical loading cycle makes shape memory alloys (SMAs) very popular for applications in aerospace industry, medical devices, consume products, and other engineering fields. The underlying mechanism for the shape memory and superelastic effects, martensitic phase transformation, has been studied both theoretically and experimentally [1–5]. Recent work has started to explore these effects at the micro- and nanoscales for both single crystal and polycrystalline structures [6–8]. These studies have revealed some interesting size-dependent responses of copper-based SMAs and NiTi. For Cu-13.7 Al-5 Ni (wt.%) micro- and nanopillars subject to compressive loading, it has been shown that the stress hysteresis increases significantly as the diameter of the pillar decreases [9]. The same effect has been observed in oligocrystalline Cu-13.7 Al-5 Ni (wt.%) and Cu-22.9 Zn-6.3 Al (wt.%) microwire tension tests [7, 10, 11]. For bulk nanocrystalline Ni-50.3 at%Ti, it has been shown that thermally induced martensitic phase transformation is suppressed in grains with diameter less than 50 nm [12]. In addition, compression tests on single crystal Ti-50.9 at.%Ni pillars have shown that the strain recovery diminishes with the pillar diameter and is suppressed for pillars with diameter smaller than about 200 nm [13]. Further study has revealed that this trend of losing superelasticity at small pillar sizes does not depend on the crystal orientations [14]. Different explanations of this size-dependent behavior have been proposed. In-situ compression tests have provided evidence of stress-induced martensitic phase transformation in NiTi pillars with diameter below 200 nm [15], which rules out the possible explanation that stress-induced martensitic

2

phase transformation may be absent at this length scale. Focused ion beam (FIB) machining that is commonly used to prepare these small pillars will leave a Ga^+ implanted outer layer about 10 nm in thickness, and it is hypothesized that this damaged layer could significantly affect the mechanical response of NiTi pillars when this outer layer thickness is comparable to the pillar diameters [13]. Unfortunately, the mechanical properties of this Ga^+ implanted NiTi layer are not available, which prevents further quantitative investigation. Another explanation comes from the consideration of the surface Ti oxide layer [13, 16], which has been shown to constrain the thermally induced martensitic phase transformation in thin films [17, 18]. This Ti oxide layer about 15 nm in thickness does not participate in the phase transformation, and also creates a Ti-depleted zone about 50 nm in thickness [16, 17, 19], which has limited ability for the phase transformation since the increase in the Ni content stabilizes the austenitic phase [1, 20]. For very small pillars, Fig 1, the fixed-thickness Ti oxide layer and Ti-depleted zone take most of the pillar volume, and the suppression of superelasticity can be expected. In this work, we attempt to provide a model-based quantitative study on how this Ti oxide layer affects the mechanical behavior of NiTi pillars under compression, giving special emphasis to the size-dependent incomplete strain recovery observed experimentally.

In the past, a large number of thermomechanical material models have been developed for SMAs. A comprehensive review of these efforts can be found in [5]. However, only a few address size effects: Sun and He proposed a 2D strain gradient viscoelastic model to simulate the grain-size dependence of stress hysteresis in bulk nanocrystalline NiTi [21]; Qiao et al. proposed
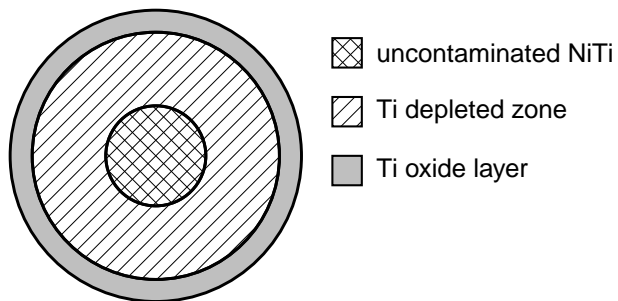
Figure 1: Schematic cross-section of a NiTi nanopillar with Ti oxide layer and Ti-depleted zone.

a 1D gradient plasticity model to study the size-dependent strain hardening and stress hysteresis in single crystal Cu-Al-Ni [22]; Petryk et al. developed a model of evolving martensitic microstructures to describe the grain-size dependence of stress hysteresis [23, 24]; and Waitz et al. studied the suppression of thermally induced martensitic phase transformation in the nanograins using an inclusion model [12]. There have also been a few papers addressing incomplete strain recovery for SMAs: Yu et al. incorporated plasticity in their austenite model at high temperature when slip becomes active [25]; Yan et al. incorporated plasticity in martensite to study the stabilization of martensite due to slip [26]; Lagoudas et al. modeled the saturation of residual strain under cyclic loading, where the plastic strain rate was assumed to be proportional to the rate of detwinned martensitic volume fraction [27, 28].

The modeling approach adopted in this paper treats the NiTi pillars as a composite material comprising a uncontaminated NiTi core, and an external Ti oxide layer. We propose a nonlocal superelastic model for the NiTi core, and an elastoplastic model for the Ti oxide layer. Through Voigt-average analysis and finite element simulations, these models are used to investigate

4

the quantitative influence of the Ti oxide layer on the mechanical responses of NiTi pillars under cyclic compression loading. The simulation results show that the plastic deformation in the Ti oxide layer constrains the recovery of deformation in the whole pillar, and the effect becomes severe with diminishing pillar size. The agreement with experimental results suggests that the size-dependent strain recovery and the loss of superelasticity in small pillars are likely to be associated with the plastic deformation in the Ti oxide layer.

2. Model

The NiTi pillar consists of a Ti oxide layer (mainly TiO_2 [17, 29]), a Ti-depleted zone and an uncontaminated NiTi SMA core, Fig. 1. The Ti-depleted zone is expected to behave as a smooth transition from Ti oxide to NiTi SMA. Due to the lack of material properties for this region, we investigate the two bounding cases in which the Ti-depleted zone is either full NiTi or full TiO_2. The TiO_2 layer has, respectively, a thickness of 15 and 65 nm. Material models for the NiTi SMA and TiO_2 will be discussed in the following subsections.

2.1. NiTi SMA – nonlocal superelasticity

We assume for simplicity isotropic response for both elastic and superelastic effects. Specifically, we ignore the dependency of the elastic moduli, the critical stresses for phase transformation, the maximum phase transformation strain, and the phase transformation strain-hardening on crystal orientation. For definiteness, we calibrate our model parameters to one specific composition and orientation. In our model, the displacement $\mathbf{u}$ and the martensitic volume fraction ξ are the two primary unknown fields. The total

strain $\mathbf{E} = \frac{1}{2}(\nabla\mathbf{u} + (\nabla\mathbf{u})^\tau)$, where ∇ denotes the spatial gradient and $()^\tau$ denotes the transpose, is decomposed into an elastic part $\mathbf{E}^e$ and a phase transformation part $\mathbf{E}^t$:

$$\mathbf{E} = \mathbf{E}^e + \mathbf{E}^t . \tag{1}$$

The evolution of the phase transformation strain $\mathbf{E}^t$ is assumed to follow the relation

$$\dot{\mathbf{E}}^t = \dot{\xi}\Lambda^t \tag{2}$$

where Λ^t is the phase transformation flow direction, and $\dot{()}$ denotes temporal derivatives. Following [30], Λ^t takes the following form

$$\Lambda^t = \begin{cases} \sqrt{\frac{3}{2}}\bar{\varepsilon}^t \frac{\mathbf{S}^{\mathrm{dev}}}{\|\mathbf{S}^{\mathrm{dev}}\|} , & \text{for } \dot{\xi} > 0 \\ \sqrt{\frac{3}{2}}\bar{\varepsilon}^t \frac{\mathbf{E}^{t,r}}{\|\mathbf{E}^{t,r}\|} , & \text{for } \dot{\xi} < 0 \end{cases} \tag{3}$$

where $\mathbf{S}^{\mathrm{dev}}$ is the deviatoric part of the Cauchy stress tensor $\mathbf{S}$, the scalar $\bar{\varepsilon}^t$ is the maximum transformation strain along the loading direction, and $\mathbf{E}^{t,r}$ is the phase transformation strain tensor upon unloading.

The free energy per unit volume consists of the elastic, chemical, hardening and nonlocal terms

$$\psi^{\mathrm{NiTi}} = \frac{1}{2}(\mathscr{C} : \mathbf{E}^e) : \mathbf{E}^e - \Delta s_{\mathrm{eq}}(T - T_{\mathrm{eq}})\xi$$
$$+ \frac{1}{2}H^t(\xi)^2 + \frac{1}{2}S_0\ell_e^2\|\nabla\xi\|^2 . \tag{4}$$

The elastic tensor $\mathscr{C}$ is the arithmetic average of the corresponding elastic moduli for austenite and martensite, i.e. $\mathscr{C} = (1 - \xi)\mathscr{C}^A + \xi\mathscr{C}^M$. T_{eq} is the equilibrium temperature between the two phases in the stress-free state, Δs_{eq} is the entropy for phase transformation from austenite to martensite at T_{eq}, and T is the temperature at which the experiments are performed. The

6

hardening parameter H^t has dimensions of stress and characterizes the classic strain-hardening during phase transformation. The nonlocal term accounts for the interfacial energy between the two phases. S_0 is a model parameter with dimensions of stress, and ℓ_e is the energetic length scale. Introducing the gradient of the martensitic volume fraction ξ in the free energy leads to an extra governing partial differential equation (micro-force equilibrium) in addition to the classic force balance equation, both of which follow directly from the principle of virtual power [31]. Consider any sub-domain V of the NiTi SMA. The internal power expended on V can be expressed as

$$\mathcal{P}^{int}(\dot{\mathbf{E}}^e, \dot{\xi}) = \int_V \mathbf{S} : \dot{\mathbf{E}}^e + k\dot{\xi} + \mathbf{k}^{nl} \cdot \nabla\dot{\xi} \, d\mathbf{x} \tag{5}$$

where k and $\mathbf{k}^{nl}$ are the work-conjugate variables to $\dot{\xi}$ and $\nabla\dot{\xi}$, respectively. The external power expended on V can be expressed by

$$\mathcal{P}^{ext}(\dot{\mathbf{u}}, \dot{\xi}) = \int_{\partial V} \hat{\mathbf{t}} \cdot \dot{\mathbf{u}} + \hat{k}\dot{\xi} \, d\mathbf{x} \tag{6}$$

where ∂V is the surface of V, $\hat{\mathbf{t}}$ and $\hat{k}$ are the traction and micro-traction, respectively. Principle of virtual power states that

$$\mathcal{P}^{int}(\check{\dot{\mathbf{E}}}^e, \check{\dot{\xi}}) = \mathcal{P}^{ext}(\check{\dot{\mathbf{u}}}, \check{\dot{\xi}}) \tag{7}$$

for any general velocity $(\check{\dot{\mathbf{u}}}, \check{\dot{\xi}}, \check{\dot{\mathbf{E}}}^e)$ satisfying the kinematic requirement $\check{\dot{\mathbf{E}}} = \frac{1}{2}(\nabla\check{\dot{\mathbf{u}}} + (\nabla\check{\dot{\mathbf{u}}})^\tau) = \check{\dot{\mathbf{E}}}^e + \check{\dot{\mathbf{E}}}^t = \check{\dot{\mathbf{E}}}^e + \check{\dot{\xi}}\Lambda^t$. Integrating by parts and using the symmetry of the stress tensor $\mathbf{S}$, the left hand side of Eq. (7) can be rewritten as

$$\mathcal{P}^{int}(\check{\dot{\mathbf{E}}}^e, \check{\dot{\xi}}) = \int_V (-\nabla \cdot \mathbf{S}) \cdot \check{\dot{\mathbf{u}}} + (-\mathbf{S} : \Lambda + k - \nabla \cdot \mathbf{k}^{nl})\check{\dot{\xi}} \, d\mathbf{x}$$
$$+ \int_{\partial V} (\mathbf{S} \cdot \mathbf{n}) \cdot \check{\dot{\mathbf{u}}} + (\mathbf{k}^{nl} \cdot \mathbf{n})\check{\dot{\xi}} \, d\mathbf{x} \tag{8}$$

7

where $\mathbf{n}$ is the unit outer normal to the surface ∂V. Since Eq. (7) must hold for any admissible field $\dot{\mathbf{u}}$ and $\dot{\xi}$, the following two partial differential equations are obtained: the macro-force balance equation

$$\nabla \cdot \mathbf{S} = 0 \,, \tag{9}$$

and the micro-force balance equation

$$\mathbf{S} : \Lambda^t - k + \nabla \cdot \mathbf{k}^{nl} = 0 \,, \tag{10}$$

as well as the following two boundary conditions: $\mathbf{S} \cdot \mathbf{n} = \hat{\mathbf{t}}$ and $\mathbf{k}^{nl} \cdot \mathbf{n} = \hat{k}$ on ∂V. The second law of thermodynamics requires that the temporal increase in the free energy cannot exceed the externally expended power:

$$\overline{\int_V \psi^{\mathrm{NiTi}} \, d\mathbf{x}} \leq \mathcal{P}^{ext} \,. \tag{11}$$

The temporal increment in free energy density can be expressed as $\dot{\psi}^{\mathrm{NiTi}} = \frac{\partial \psi^{\mathrm{NiTi}}}{\partial \mathbf{E}^e} : \dot{\mathbf{E}}^e + \frac{\partial \psi^{\mathrm{NiTi}}}{\partial \xi} \dot{\xi} + \frac{\partial \psi^{\mathrm{NiTi}}}{\partial (\nabla \xi)} \cdot \nabla \dot{\xi}$. It then follows that

$$0 \leq (\mathbf{S} - \frac{\partial \psi^{\mathrm{NiTi}}}{\partial \mathbf{E}^e}) : \dot{\mathbf{E}}^e + (k - \frac{\partial \psi^{\mathrm{NiTi}}}{\partial \xi}) \dot{\xi}$$
$$+ (\mathbf{k}^{nl} - \frac{\partial \psi^{\mathrm{NiTi}}}{\partial (\nabla \xi)}) \cdot \nabla \dot{\xi} \,. \tag{12}$$

Inspired by the strain gradient plasticity theory in [31], the constitutive relations for the work-conjugate variables are defined as $\mathbf{S} = \frac{\partial \psi^{\mathrm{NiTi}}}{\partial \mathbf{E}^e}$, $k = \frac{\partial \psi^{\mathrm{NiTi}}}{\partial \xi} + Y \mathrm{sign}(\dot{\xi})$, and $\mathbf{k}^{nl} = \frac{\partial \psi^{\mathrm{NiTi}}}{\partial (\nabla \xi)}$, where the model parameter Y which has dimensions of stress characterizes the resistance to phase transformation. The first constitutive relation represents the classic Hooke's law

$$\mathbf{S} = \mathscr{C} : \mathbf{E}^e \,. \tag{13}$$

With the newly derived constitutive relations, Eq. (10) can be rewritten as

$$Y\text{sign}(\dot{\xi}) = \mathbf{S} : \Lambda^t - \frac{1}{2}(\frac{\partial\mathscr{C}}{\partial\xi} : \mathbf{E}^e) : \mathbf{E}^e + \Delta s_{\text{eq}}(T - T_{\text{eq}})$$
$$- H^t\xi + S_0\ell_e^2(\nabla\cdot\nabla)\xi , \tag{14}$$

where the left hand side can be viewed as the resistance to the phase transformation, i.e. $\pm Y$ for the forward and reverse transformation respectively, and the right hand side can be viewed as the driving force for the phase transformation. In the absence of the gradient term, Eq. 14) represents the conventional local phase transformation conditions [30].

2.2. Ti oxide – plasticity

The TiO$_2$ layer is modeled as isotropic elastic-perfectly plastic material. The decomposition of the total strain tensor now reads

$$\mathbf{E} = \mathbf{E}^e + \mathbf{E}^p , \tag{15}$$

where $\mathbf{E}^p$ is the plastic strain tensor. The evolution of $\mathbf{E}^p$ follows the flow rule

$$\dot{\mathbf{E}}^p = \dot{\varepsilon}^p\Lambda^p , \tag{16}$$

where $\dot{\varepsilon}^p$ denotes the equivalent plastic strain rate, and Λ^p is the plastic flow direction, which takes the normality rule

$$\Lambda^p = \sqrt{\frac{3}{2}}\frac{\mathbf{S}^{\text{dev}}}{\|\mathbf{S}^{\text{dev}}\|} . \tag{17}$$

The constitutive relations include Hooke's law,

$$\mathbf{S} = \mathscr{C}^O : \mathbf{E}^e , \tag{18}$$

where $\mathscr{C}^O$ is the elastic moduli of TiO$_2$, and the conventional J_2 plastic yield condition,

$$\sqrt{\frac{3}{2}}\|\mathbf{S}^{\text{dev}}\| - \bar{\sigma}_y = 0 \ , \tag{19}$$

where $\bar{\sigma}_y$ is the compressive yield strength.

The plastic hardening of TiO$_2$ is ignored because it is expected to be much smaller than the strain-hardening rate of NiTi SMA. The fixed-thickness TiO$_2$ layer is supposed to dominate in the small pillars, while it has been observed that pillars with diameter smaller than 200 nm exhibit less strain-hardening than pillars with larger diameters, and the 162 nm [210] oriented pillar even shows a perfect plateau [14].

2.3. Model parameters

The values of the SMA model parameters are determined for [111] oriented Ti-50.9at%Ni, for which the size dependence of the strain recovery is observed [13]. The elastic moduli are taken from the estimation of the corresponding bulk material with the austenite Young's modulus $E^A = 59$ GPa, and the austenite Poisson's ratio $\nu^A = 0.3$ [13]. The elastic properties of martensite are assumed to be the same as those of austenite, i.e. $E^M = E^A = 59$ GPa, $\nu^M = \nu^A = 0.3$. The equilibrium temperature $T_{\text{eq}} = 200$ K, and the transformation entropy $\Delta s_{\text{eq}} = $ -4.05 J·mol^{-1}·K$^{-1}/(a_0^3 N_A) = $ -0.245 MPa·K^{-1} are obtained from [20], where $a_0 = 0.3015$ nm is the lattice parameter of the austenite NiTi at room temperature [32], and N_A is the Avogadro constant. The maximum transformation strain $\bar{\varepsilon}^t = 0.036$ is obtained from [33]. The transformation resistance, Y, is calculated through

the 1D degenerate case of the micro-force balance equation, Eq. (14),

$$Y \operatorname{sign}(\dot{\xi}) = \sigma \bar{\varepsilon}^t + \Delta s_{\text{eq}}(T - T_{\text{eq}}) - H^t \xi \,, \tag{20}$$

where σ is the stress along the loading direction. At $T = 298$ K, a stress value 800 MPa has been reported as the point in which the forward martensitic phase transformation initiates [14, 33]. $Y = 4.6$ MPa is then obtained by applying the values of the parameters above. The hardening coefficient H^t is derived from the experimental strain-hardening rate in the following way. From Eq. (20), one obtains $\frac{\partial \sigma}{\partial \varepsilon} \bar{\varepsilon}^t - H^t \frac{\partial \xi}{\partial \varepsilon} = 0$ by taking the derivative with respect to the total strain ε. From Eq. (13), one obtains $\frac{\partial \sigma}{\partial \varepsilon} = E(1 - \frac{\partial \xi}{\partial \varepsilon} \bar{\varepsilon}^t)$ with assumption $E = E^A = E^M$. Combining these two equations leads to $H^t = \frac{\partial \sigma}{\partial \varepsilon} (\bar{\varepsilon}^t)^2 / (1 - \frac{1}{E} \frac{\partial \sigma}{\partial \varepsilon})$. By replacing $\frac{\partial \sigma}{\partial \varepsilon}$ with the experimentally reported value 20 GPa [14], $H^t = 39.2$ MPa is obtained.

The group of parameters $S_0 \ell_e^2$ has the effect to enhance the strain-hardening rate for nonuniform phase transformations [22]. In this study, the values, $S_0 \ell_e^2 = 0.01$ nm$^2 E^A$ and 1 nm$^2 E^A$, will be adopted to study this effect.

Material parameters for TiO$_2$ including the Young's modulus $E^O = 287$ GPa, the Poisson's ratio $\nu^O = 0.268$, and the compressive yield strength $\bar{\sigma}_y = 3$ GPa are obtained from [34].

2.4. Composite Voigt-average model

In the analysis of composite materials, Voigt average, which assumes uniform strains, is commonly used to estimate the stiffness and the stresses. In this work, we also employ it to analyze the response of the composite NiTi/TiO$_2$ pillars. Consider a NiTi pillar with diameter D that contains a TiO$_2$ layer with thickness t^O. The strain along the loading direction ε is
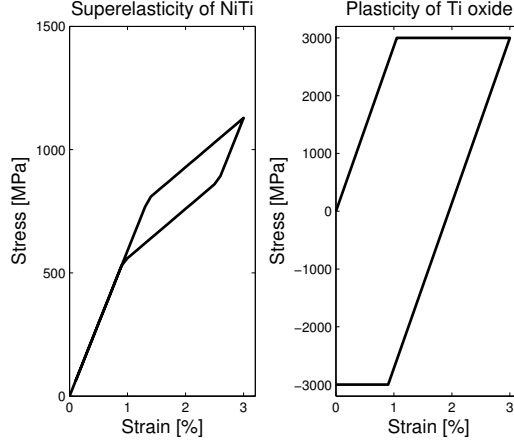
Figure 2: Compressive stress-strain curves of NiTi SMA and TiO$_2$ under a uniaxial loading cycle with maximum strain 3%.

assumed identical in the two materials. Given a strain history, the stress along the loading direction within each material, σ^{NiTi} and σ^O, can be calculated independently using its constitutive relations, Eq. (13), (20), (18) and (19), where the gradient term in the NiTi SMA model is ignored. Fig. 2 plots the stress-strain curves of NiTi SMA and TiO$_2$ during a compressive loading cycle with maximum strain 3%. Complete strain recovery and stress hysteresis in the strain-loading cycle can be observed in the response of NiTi SMA. For TiO$_2$, one can observe the typical strain-cycle response for an elastic perfectly-plastic material leading to a residual stress when the strain goes back to zero. The reaction force from the pillar cross-section, f, is the sum of the reaction forces from the two materials, i.e.

$$f = \pi \left(\frac{D}{2} - t^O \right)^2 \sigma^{\text{NiTi}} + \pi \left[\left(\frac{D}{2} \right)^2 - \left(\frac{D}{2} - t^O \right)^2 \right] \sigma^O . \qquad (21)$$

And the average stress response of the composite can be obtained as follows

$$\sigma = \frac{f}{\pi \left(\frac{D}{2}\right)^2} = w\sigma^{\text{NiTi}} + (1-w)\sigma^O \ , \tag{22}$$

where the weight w is defined as

$$w = \left[1 - 2\left(\frac{t^O}{D}\right)\right]^2 \ . \tag{23}$$

The results using this model are shown in Section 3.

2.5. Finite element model

The composite model presented in the previous section does not consider the interaction between the TiO_2 layer and the NiTi core, and in particular ignores the constraint from the TiO_2 layer on the martensitic phase transformation in NiTi SMA. In addition, due to the locality of the constitutive models for the TiO_2 plasticity and the SMA superelasticity, the homogenized approach can only capture size effects through the volume ratio of the two components but will be insensitive to a change of the spatial scale.

In order to explore the role of the interaction between the two components including gradient effects at the TiO_2-NiTi interface produced by the internal constraint to the phase transformation, three-dimensional finite element calculations are performed using the full nonlocal SMA model. The pillar is modeled as a cylinder of diameter D and height h. Due to symmetry, only a quarter of the pillar is considered in the computation, Fig 3. In reality, the top surface is also covered by the TiO_2 layer, which could significantly affect the mechanical response if the aspect ratio h/D is small. It has been reported that the aspect ratio of all samples ranges between 1.6 and 3.9 [13], although no such information for individual pillar is provided. For simplicity,
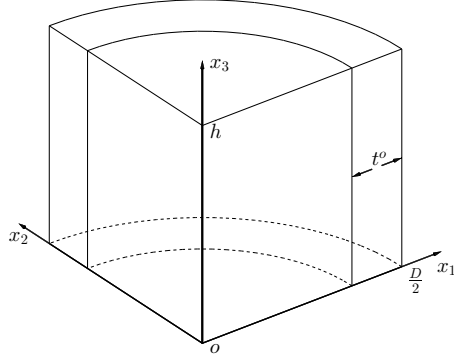
13

Figure 3: Quarter pillar for finite element calculations.

we ignore this top TiO_2 layer, and focus on the size effect related to changes in the diameter. A fixed pillar height $h = 100$ nm is then assumed for all the pillars in the finite element simulations. Due to the gradient terms, the micro-force balance equation for NiTi SMA, Eq. (14), is a partial differential equation of the martensitic volume fraction, and is coupled with the macro-force balance equation, Eq. (9). With proper boundary conditions, these two equations for NiTi SMA, and the governing equation for TiO_2 (same as Eq. (9)), complete the formulation of the pillar compression test boundary value problem. A finite element discretization with a staggered coupled scheme is used to approximate the resulting coupled macro- and micro-force balance equations in weak form.

3. Results and Discussion

For both the composite Voigt-average and the finite element models, the experiments are simulated as follows. Since both the superelasticity and the plasticity are history-dependent, the strain history is applied in increments of
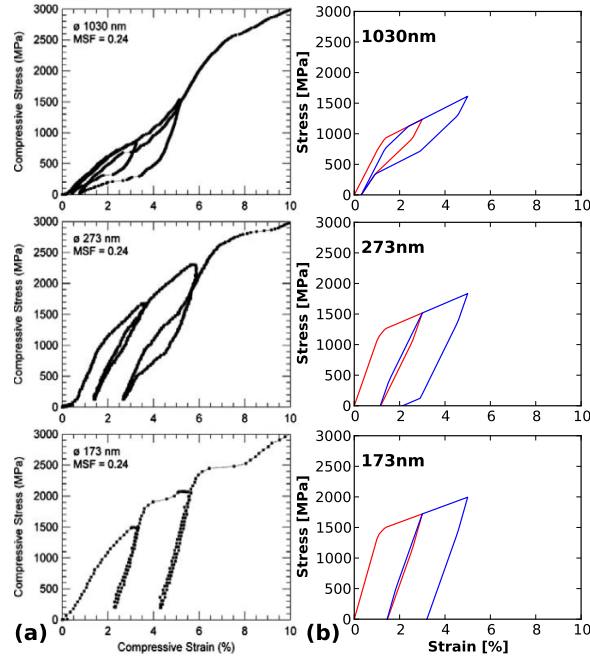
14

Figure 4: Compressive stress-strain curves from (a) experiments [14] and (b) Voigt-average analysis. Red and blue colors indicate the first and second loading cycles, respectively.

0.1%, and at each strain increment the constitutive models are integrated numerically. Following the experimental conditions, the strain is first increased to -3%, and then decreased until the reaction force becomes zero. The pillar is then reloaded to -5% strain, and unloaded until the reaction force becomes zero again. The evolution of the stress, the martensitic volume fraction (NiTi SMA) and the plastic strain (TiO_2) are recorded during the entire procedure. The strain history is applied at a constant temperature $T = 298$ K.

3.1. Voigt-average model

In Fig 4, the stress-strain curves from the composite Voigt-average model are compared to the experimental results for pillars with diameter 1030, 273,
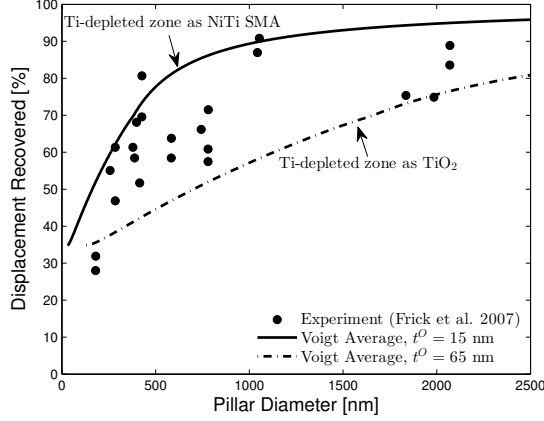
Figure 5: Comparison of experiments and Voigt-average of two extreme TiO$_2$ thicknesses for the displacement recovery during the first loading cycle.

and 173 nm. In these calculations, the TiO$_2$ layer thickness t^O is taken as 15 nm. The simulations reproduce some important features of the experimental results. First, the residual strain at the end of the first loading cycle increases significantly as the pillar diameter decreases. For the smallest diameter (173 nm) there is essentially no strain recovery except for the elastic response, which indicates that in this case the superelastic effect is suppressed. By contrast, the 1030 nm pillar almost completely recovers its deformation. The medium-size pillar (273 nm) shows an intermediate response between these two limits with some strain recovery. It can also be observed that the stress hysteresis between the intermediate unloading and reloading clearly decreases as the pillar diameter decreases.

Fig. 5 shows a summary of the experimentally-observed displacement recovery as a function of pillar diameter as well as the predictions from the Voigt model for two extreme TiO$_2$ layer thicknesses. Two values of the
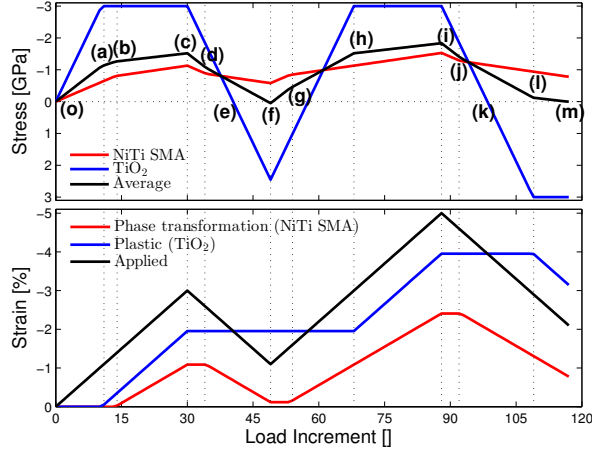
16

Figure 6: Evolution of the stresses (top) and the strains (bottom) for the 273 nm pillar from Voigt-average analysis.

TiO$_2$ layer thickness, 15 and 65 nm, are used as described in Section 2. It can be seen that the model captures the decrease in the displacement recovery for decreasing pillar size and that the extreme cases in which the Ti-depleted zone is considered as full NiTi and TiO$_2$ provide nice bounds for the experimental values. For very small pillar diameters, the two TiO$_2$ layer thicknesses considered give an identical limit value of the recovered displacement $\bar{\sigma}_y/(E^O 3\%) \approx 34.8\%$, which represents the response of pure TiO$_2$.

In order to gain more insight into the model response, in Fig. 6 we plot the stress and strain history experienced by each material component as well as the macroscopic average value as a function of load increment for the case of the 273 nm pillar with TiO$_2$ thickness 15 nm. More specifically, we show the stress in NiTi, the stress in TiO$_2$, and the average stress, Eq. (22); we also show the applied strain, which is identical in the two materials, the phase

17

transformation strain in NiTi, and the plastic strain in TiO_2. The elastic strains are not shown as they can be directly derived from the stresses in the two materials. Singular points in the load history have been identified with letters to facilitate the discussion. During the first thirty load increments in which the applied strain is increased up to -3%, we can first observe the elastic loading up to point (a) (-1% applied strain) when TiO_2 starts to yield plastically, followed by the onset of transformation in NiTi SMA at (b) (-1.4%). Continued loading promotes the development of the phase transformation strain and the plastic strain until (c) where the applied strain reaches the prescribed maximum. At point (c) when unloading begins both components experience elastic unloading until (d) when the NiTi SMA starts the reverse phase transformation. It is worth noting that at point (e) during the elastic unloading the stress in TiO_2 vanishes before the average stress does and becomes tensile with further decrease of the applied strain. At (f), the average stress reaches zero and the first loading cycle is complete with a residual strain of about -1.1%; residual stresses of about 2.5 GPa (tensile) and -0.6 GPa (compressive) remain in TiO_2 and NiTi SMA, respectively; the residual plastic strain in TiO_2 is about -2%, whereas the residual phase transformation strain in NiTi SMA is about -0.1%. During the second loading cycle the applied strain is increased from its residual value to -5% (i). There is first elastic reloading up to (g) where the forward phase transformation begins, whereas TiO_2 continues to load elastically up to (h) where plastic yielding starts again. Both the phase transformation strain and the plastic strain continue developing until the applied strain reaches the prescribed maximum at (i). Subsequent unloading from (i) proceeds elastically until
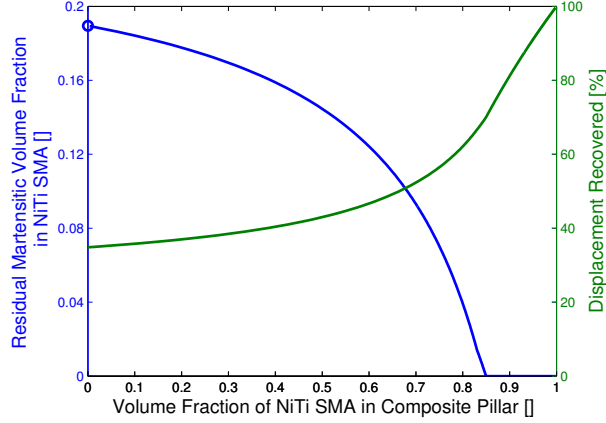
Figure 7: Residual martensitic volume fraction in NiTi SMA and the percentage of displacement recovery at the end of first loading cycle.

the reverse phase transformation of NiTi SMA starts at (j). At (k), the stress in TiO_2 becomes tensile as in the first loading cycle and grows to the point (l) where plastic yielding under tension starts. At (m), the average stress eventually decreases to zero, and the second loading cycle is complete with a residual strain about -2.1%; residual stresses of about 3 GPa (tensile) and -0.78 GPa (compressive) remain in TiO_2 and NiTi SMA, respectively; the residual plastic strain in TiO_2 is about -3.2%, whereas the residual phase transformation strain in NiTi SMA is about -0.8%.

Further insights can be obtained from the Voigt-average model. For example, Fig. 7 shows the residual martensitic volume fraction in NiTi SMA and the displacement recovery at the end of the first loading cycle as a function of the volume fraction of NiTi SMA in the composite pillar, i.e. w defined in Eq. (23). It can be seen that the residual martensitic volume fraction decreases as w increases, and eventually vanishes at $w = 0.85$. For a fixed

TiO$_2$ thickness, it means that the stress-induced martensite does not fully transform back to the austenite in small pillars; the amount of the residual martensite decreases with increasing pillar size; and the reverse transformation will be complete for pillars with the volume fraction of NiTi SMA above 0.85. It can also be seen that the displacement recovery increases monotonically with w. When $w = 0$, the displacement recovery equals $\bar{\sigma}_y/(E^O 3\%)$, which represents the pure TiO$_2$ response. When $w = 1$, the displacement recovery is 100%, which represents the pure NiTi SMA response. The curve is steepest for w above 0.8, which indicates that the displacement recovery is most sensitive within this range.

3.2. Finite element simulations

As mentioned in Section 2.5, we have also conducted three-dimensional finite element simulations using the nonlocal SMA model in order to explore possible additional size effects resulting from the constraint to phase transformation at the TiO$_2$-NiTi interface.

The following boundary conditions are adopted to simulate the pillar compression tests: $u_i = 0$ at $x_i = 0$ for $i = 1, 2, 3$, and $u_3 = \hat{u}_3$ at $x_3 = h$. The displacement $\hat{u}_3$ is prescribed to match the strain history in the experiments. At the TiO$_2$-NiTi interface $((x_1^2 + x_2^2)^{\frac{1}{2}} = D/2 - t^O)$, we constrain the martensitic phase transformation with the boundary condition in the micro-force balance equation (10) by setting the martensite volume fraction $\xi = 0$.

In Fig. 8, stress-strain curves extracted from finite element simulations for three pillar diameters with TiO$_2$ thickness of 15 nm and the nonlocal energetic coefficient $S_0 \ell_e^2 = 1 \, \text{nm}^2 E^A$ are compared with the Voigt-average
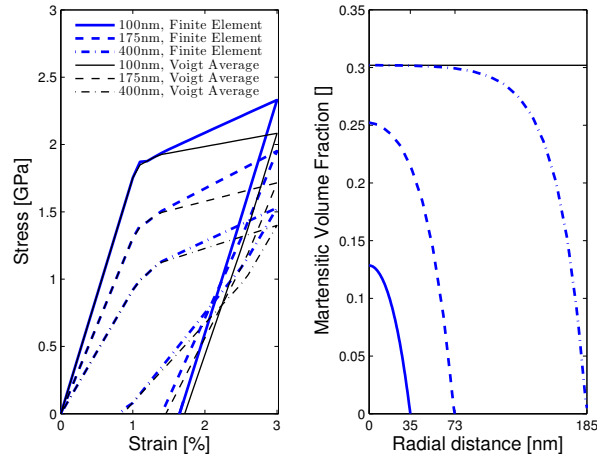
Figure 8: Compressive stress-strain curves of 100, 175, 400 nm pillars during the first loading cycle, and the distribution of martensitic volume fraction along pillar radius when first loaded to 3% strain.

results. It can be seen that the finite element model has also captured the feature of increasing residual strain for decreasing pillar size, and the residual strains predicted are very close to the Voigt-average results. It is also clear in both the finite element and Voigt-average results, that the apparent elastic modulus and the yield stress increase for decreasing pillar size. This can be attributed to the increasing proportion of TiO_2, whose Young's modulus and yield strength are larger than the Young's modulus and the critical stress of the NiTi SMA, respectively. The finite element results also show an enhanced strain-hardening compared to the Voigt-average results, as expected from the nonlocal SMA model [22]. In Fig. 8, we also plot the martensitic volume fraction along the radial direction at the maximum applied strain. It can be seen that the Voigt model has predicted an identical value about 0.3 for the three pillar sizes, whereas the martensitic volume fraction predicted by
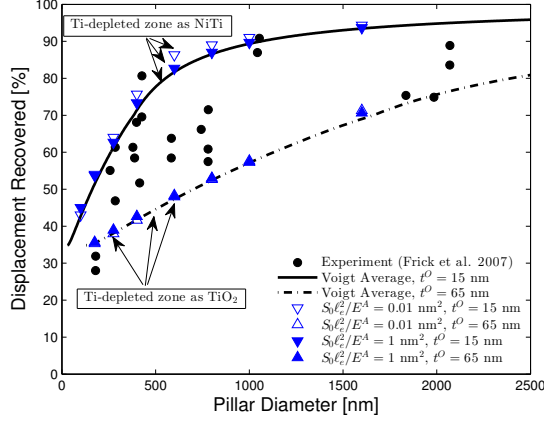
21

Figure 9: Displacement recovery during the first loading cycle extracted from finite element simulations in comparison with experiments and Voigt-average results.

the finite element model decreases, and the relative area of influence of the TiO$_2$-NiTi interface expands for decreasing pillar size.

In Fig. 9, we summarize the displacement recovery at the end of the first loading cycle predicted by the finite element model for a wide range of pillar diameters, and compare it with the experiments and the predictions of the Voigt-average model. It can be seen that the displacement recovery predicted by the finite element model for the two representative values of $S_0\ell_e^2$ is very close to and sometimes even coincides with the corresponding prediction of the Voigt-average model. Since the nonlocal energy and the interaction between the NiTi SMA and TiO$_2$ are not considered in the Voigt-average model, the match suggests that these two factors have a negligible impact on the amount of the displacement recovery.

In [14], the experimental stress-strain curves have shown that the strain-hardening rate during the phase transformation is highest for medium-size
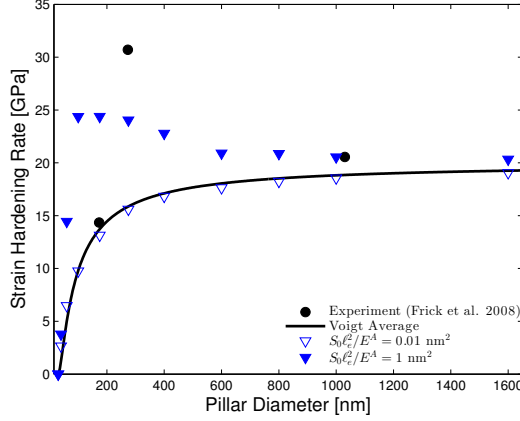
Figure 10: Strain-hardening rate during the phase transformation extracted from finite element simulations in comparison with experiments and Voigt-average results.

pillars with diameter between 200 and 400 nm, and the differences in the strain-hardening rate are attributed to the taper shape of the individual pillar. However, this explanation has not been further quantified. In this study, we proceed to interpret the experimental observations with our model, which suggests a pillar-size dependence on the strain-hardening rate. In Fig. 10, the strain-hardening rate extracted from the finite element simulations with TiO_2 thickness of 15 nm and two representative values of $S_0\ell_e^2$ are compared with those extracted from the experiments and the Voigt-average results. For the finite element simulations with $S_0\ell_e^2/E^A = 1\,\text{nm}^2$, it can be seen that starting from large pillar sizes, the strain-hardening rate first increases for decreasing pillar size, and at about 200 nm it starts to decrease with further decrease in the pillar size, which is consistent with the experimental observations. It has been shown in [22] that for pure SMA, the hardening effect increases for decreasing pillar size due to the nonlocal term in the free energy

and the constraint of phase transformations. However, because of the presence of the TiO_2 layer, in smaller and smaller pillars, the strain-hardening rate eventually drops as it approaches the perfect plastic response. For the finite element simulations with much smaller $S_0\ell_e^2$, the enhancement of the strain-hardening rate due to the nonlocal energy is negligible, and the result simply coincides with the prediction from the Voigt-average model, which decreases monotonically with decreasing pillar size.

4. Conclusions

In this work, we have proposed an approach to model the NiTi nanopillars subject to cyclic compressive loadings. The NiTi pillars have been treated as a composite material comprising a NiTi SMA core, and a TiO_2 outer layer, whose thickness is assumed to be fixed regardless of pillar sizes. A nonlocal superelastic material model with the gradient of the martensitic volume fraction in the free energy has been used for NiTi SMA, and an elastoplastic material model has been used for TiO_2. Composite Voigt-average analysis and finite element calculations have been performed to study the role of the TiO_2 layer in the cyclic compression tests of NiTi pillars.

Both Voigt-average and finite element simulations have captured the experimental observation of the loss of superelasticity in the small pillars. It has been shown that the plastic deformation in the TiO_2 layer prevents the complete strain recovery of the pillar during unloading, an effect that is more noticeable for smaller pillar sizes, i.e. as the TiO_2 layer takes more of the pillar volume. This results in the increase of both the residual strain and the residual martensitic volume fraction for decreasing pillar size.

The finite element simulations have also provided an explanation of the experimentally observed size dependence on the strain-hardening rate during the phase transformation, where the strain-hardening rate first increases and then decreases with decreasing pillar size. In large pillars, where NiTi SMA occupies most of the volume, the nonlocal energy together with the confinement from the TiO_2 layer on the phase transformation causes the increase of the strain-hardening rate for decreasing pillar size. In very small pillars, where the TiO_2 layer occupies relatively more volume, the response approximates the perfect plasticity, leading to the drop of the strain-hardening rate.

Acknowledgments

References

[1] Otsuka, K., Wayman, C.M., editors. Shape memory materials. Cambridge University Press; 1998.

[2] Bhattacharya, K.. Microstructure of martensite: why it forms and how it gives rise to the shape-memory effect. Oxford University Press; 2003.

[3] Roubíček, T.. Models of microstructure evolution in shape memory alloys. In: Castaeda, P., Telega, J., Gambin, B., editors. Nonlinear Homogenization and its Applications to Composites, Polycrystals and Smart Materials. Springer Netherlands; 2005, p. 269–304.

[4] Abeyaratne, R., Knowles, J.K.. Evolution of phase transitions: a continuum theory. Cambridge University Press; 2006.

[5] Lagoudas, D.C., editor. Shape memory alloys: modeling and engineering applications. Springer; 2008.

[6] Waitz, T., Tsuchiya, K., Antretter, T., Fischer, F.. Phase transformations of nanocrystalline martensitic materials. MRS Bull 2009;34:814–821.

[7] Chen, Y., Schuh, C.A.. Size effects in shape memory alloy microwires. Acta Mater 2011;59:537–553.

[8] Greer, J.R., Hosson, J.T.D.. Plasticity in small-sized metallic systems: Intrinsic versus extrinsic size effect. Prog Mater Sci 2011;56(6):654–724.

[9] San Juan, J., Nó, M.L., Schuh, C.A.. Nanoscale shape-memory alloys for ultrahigh mechanical damping. Nat Nanotechnol 2009;4:415–419.

[10] Ueland, S.M., Schuh, C.A.. Superelasticity and fatigue in oligocrystalline shape memory alloy microwires. Acta Mater 2012;60(1):282–292.

[11] Ueland, S.M., Chen, Y., Schuh, C.A.. Oligocrystalline shape memory alloys. Adv Funct Mater 2012;22(10):2094–2099.

[12] Waitz, T., Antretter, T., Fischer, F.D., Simha, N.K., Karnthaler, H.P.. Size effects on the martensitic phase transformation of NiTi nanograins. J Mech Phys Solids 2007;55(2):419–444.

[13] Frick, C.P., Orso, S., Arzt, E.. Loss of pseudoelasticity in nickel-titanium sub-micron compression pillars. Acta Mater 2007;55(11):3845–3855.

[14] Frick, C.P., Clark, B.G., Orso, S., Sonnweber-Ribic, P., Arzt, E.. Orientation-independent pseudoelasticity in small-scale NiTi compression pillars. Scripta Mater 2008;59(1):7–10.

[15] Ye, J., Mishra, R.K., Pelton, A.R., Minor, A.M.. Direct observation of the NiTi martensitic phase transformation in nanoscale volumes. Acta Mater 2010;58(2):490–498.

[16] San Juan, J., Nó, M.L., Schuh, C.A.. Thermomechanical behavior at the nanoscale and size effects in shape memory alloys. J Mater Res 2011;26:2461–2469.

[17] Ishida, A., Sato, M.. Thickness effect on shape memory behavior of Ti-50.0at.%Ni thin film. Acta Mater 2003;51(18):5571–5578.

[18] Fu, Y., Zhang, S., Wu, M., Huang, W., Du, H., Luo, J., et al. On the lower thickness boundary of sputtered TiNi films for shape memory application. Thin Solid Films 2006;515(1):80–86.

[19] Wang, X., Rein, M., Vlassak, J.J.. Crystallization kinetics of amorphous equiatomic NiTi thin films: Effect of film thickness. J Appl Phys 2008;103:023501.

[20] Tang, W.. Thermodynamic study of the low-temperature phase B19' and the martensitic transformation in near-equiatomic Ti-Ni shape memory alloys. Metall Mater Trans A 1997;28:537–544.

[21] Sun, Q.P., He, Y.J.. A multiscale continuum model of the grain-size dependence of the stress hysteresis in shape memory alloy polycrystals. Int J Solids Struct 2008;45:3868–3896.

[22] Qiao, L., Rimoli, J., Chen, Y., Schuh, C.A., Radovitzky, R.. Nonlocal superelastic model of size-dependent hardening and dissipation in single crystal Cu-Al-Ni shape memory alloys. Phys Rev Lett 2011;106:085504.

[23] Petryk, H., Stupkiewicz, S.. Interfacial energy and dissipation in martensitic phase transformations. Part I: Theory. J Mech Phys Solids 2010;58(3):390–408.

[24] Petryk, H., Stupkiewicz, S., Maciejewski, G.. Interfacial energy and dissipation in martensitic phase transformations. Part II: Size effects in pseudoelasticity. J Mech Phys Solids 2010;58(3):373–389.

[25] Yu, C., Kang, G., Song, D., Kan, Q.. Micromechanical constitutive model considering plasticity for super-elastic NiTi shape memory alloy. Comp Mater Sci 2012;56(0):1–5.

[26] Yan, W., Wang, C.H., Zhang, X.P., Mai, Y.W.. Theoretical modelling of the effect of plasticity on reverse transformation in superelastic shape memory alloys. Mater Sci Eng A-Struct 2003;354(1-2):146–157.

[27] Bo, Z., Lagoudas, D.C.. Thermomechanical modeling of polycrystalline SMAs under cyclic loading, Part III: evolution of plastic strains and two-way shape memory effect. Int J Eng Sci 1999;37(9):1175–1203.

[28] Lagoudas, D.C., Entchev, P.B.. Modeling of transformation-induced

plasticity and its effect on the behavior of porous shape memory alloys. Part I: constitutive model for fully dense SMAs. Mech Mater 2004;36(9):865–892.

[29] Chu, C., Wu, S., Yen, Y.. Oxidation behavior of equiatomic TiNi alloy in high temperature air environment. Mater Sci Eng A-Struct 1996;216(1-2):193–200.

[30] Boyd, J.G., Lagoudas, D.C.. A thermodynamical constitutive model for shape memory materials. Part I. The monolithic shape memory alloy. Int J Plasticity 1996;12(6):805–842.

[31] Anand, L., Gurtin, M.E., Lele, S.P., Gething, C.. A one-dimensional theory of strain-gradient plasticity: Formulation, analysis, numerical results. J Mech Phys Solids 2005;53:1789–1826.

[32] Otsuka, K., Ren, X.. Physical metallurgy of TiNi-based shape memory alloys. Progress in Materials Science 2005;50(5):511–678.

[33] Sehitoglu, H., Karaman, I., Anderson, R., Zhang, X., Gall, K., Maier, H.J., et al. Compressive response of NiTi single crystals. Acta Mater 2000;48(13):3311–3326.

[34] Carter, C.B., Norton, M.G.. Ceramic Materials Science and Engineering. Springer, New York; 2006.